Structure and Electrochemistry of Copper Fluoride Nanocomposites Utilizing Mixed Conducting Matrices

F. Badway,[†] A. N. Mansour,[‡] N. Pereira,[†] J. F. Al-Sharab,[†] F. Cosandey,[†] I. Plitz,[†] and G. G. Amatucci*,[†]

Energy Storage Research Group, Department of Materials Science and Engineering, Rutgers, The State University of New Jersey, North Brunswick, New Jersey 08902, and Systems and Materials for Power and Protection Branch, Naval Surface Warfare Center, Carderock Division, 9500 MacArthur Boulevard, West Bethesda, Maryland 20817-5700

Received February 12, 2007. Revised Manuscript Received May 24, 2007

Near-theoretical utilization of high-energy-density CuF_2 positive electrode materials for lithium batteries was enabled through the use of nanocomposites consisting of 2−30 nm domains of CuF_2 within a mixed ionic + electronic conducting matrix of a metal oxide. Small but significant crystallographic changes to the core crystal of the CuF_2 were found to occur in all oxide-based matrices. These modifications to the core crystal and the surrounding matrix were investigated through a host of characterization methods, including XRD, XPS, and XAS. This new approach to the enablement of the anhydrous CuF_2 is distinctly superior in performance to that of macro CuF_2 or CuF_2 nanocomposites utilizing carbon as a matrix, the latter of which is also introduced herein for the first time.

1. Introduction

Although widely investigated three decades ago for their high theoretical energy densities, metal fluoride compounds have been largely ignored as positive electrodes for lithium batteries because of their intrinsically poor electronic transport properties brought about by their characteristic large band gap. Recently, the possibility of reversible metal fluorides has resulted in renewed interest.[1−7] The recently introduced metal fluoride nanocomposites using carbon or metal dichalcogenide matrices has enabled the electrochemical activity of the class of high-voltage, high-energy-density metal fluorides. In contrast to the ubiquitous intercalation reaction of present day metal oxides and phosphate positive electrode materials, the reversible conversion mechanism by which some of these materials operate resulted in demonstrated specific capacities in excess of 600 mA h g^{-1} and energy densities of 1300 W h kg^{-1}. Although cycle life is limited to <50 cycles for most materials at this early stage, these materials offer an interesting path forward for next-generation positive electrode materials.

Of all the transition metal fluorides that could be enabled, one of the attractive materials is CuF_2. CuF_2 has a theoretical conversion potential of 3.55 V based on thermodynamic calculations.[8] Combining this with a theoretical discharge specific capacity of 528 mA h g^{-1} leads to an exceptionally high energy density of 1874 W h kg^{-1}. Indeed, such values are almost 300% higher than those attained in the positive electrode of present day state of the art rechargeable Li batteries based on $LiCoO_2$ intercalation compounds. With respect to existing primary cathode compounds, CuF_2 would exceed the widely utilized MnO_2 specific energy by almost a factor of 2. In addition, the CuF_2 volumetric energy density (7870 W h L^{-1}) would exceed the volumetric energy density of carbon monofluoride (approximately 6000 W h L^{-1}) with a possible advantage of faster discharge rates.

The theoretical attractiveness of the electrochemical properties of CuF_2 has been known for some time. In light of this, more than 30 years ago, a number of researchers have made an attempt to enable the electrochemical properties of this compound as a primary positive electrode. Many attempts have occurred, but none have demonstrated full utilization of this elusive compound at the appropriate voltages.[9,10] Much of the early work focused on crystalline CuF_2 with hydrated impurities such as the presence of CuOHF and $CuF_2{\cdot}2H_2O$, resulting in cells that were found to deliver only 25% of the theoretical energy density.[11] Extensive solubility of the hydrated CuF_2, with an acceptable

* Corresponding author. E-mail: gamatucc@rci.rutgers.edu.
[†] Rutgers, The State University of New Jersey.
[‡] Naval Surface Warfare Center.

(1) Li, H.; Richter, G.; Maier, J. *Adv. Mater.* **2003**, *15*, 736.
(2) Badway, F.; Pereira, N.; Cosandey, F.; Amatucci, G. G. *J. Electrochem. Soc.* **2003**, *150*, A1209.
(3) Plitz, I.; Badway, F.; Al-Sharab, J.; DuPasquier, A.; Cosandey, F.; Amatucci, G. G. *J. Electrochem. Soc.* **2005**, *152*, A307.
(4) Bervas, M.; Badway, F.; Klein, L. C.; Amatucci, G. G. *Electrochem. Solid State Lett.* **2005**, *8*, A179.
(5) Li, H.; Balaya, P.; Maier, J. *J. Electrochem. Soc.* **2004**, *151*, A1878.
(6) Bervas, M.; Klein, L. C.; Amatucci, G. G. *J. Electrochem. Soc.* **2006**, *153*, A159.
(7) Bervas, M.; Mansour, A. N.; Yoon, W. S.; Al-Sharab, J.; Badway, F.; Cosandey, F.; Klein, L. C.; Amatucci, G. G. *J. Electrochem. Soc.* **2006**, *153*, A799.
(8) Amatucci, G. G.; Pereira, N. *J. Fluorine Chem.* **2007**, *128*, 243.
(9) Bauman, H. F. Development of lithium−cupric fluoride batteries. In *Proceedings of the 20th Annual Power Sources Conference*, Fort Monmouth, NJ, May 24−26, 1966; PSC Publications: Ann Arbor, MI, 1966; p 73.
(10) Bauman, H. F. Development of the copper fluoride−lithium couple. *Proceedings of the 18th Annual Power Sources Conference*, May 19−21, 1964. Fort Monmouth, NJ; PSC Publications: Ann Arbor, MI, 1964; p 89.
(11) Bauman, H. F. In *Proceedings of the 20th Annual Power Sources Conference*, May 24−26, 1966, Fort Monmouth, NJ; PSC Publications: Ann Arbor, MI, 1966; pp 73−76.

10.1021/cm070421g CCC: $37.00
Published on Web 07/21/2007

rate capability and in some cases good utilization relative to anhydrous CuF_2, was tied with very poor stability. More importantly, voltage profiles were on the order of 2 V instead of the approximately 3 V expected through thermodynamic calculations. Two strong early efforts to develop usable CuF_2 were brought forth by Globe-Union Inc.[12] and Livingston Electric Corp.[13] The Globe-Union work examined the use of CuF_2 electrode materials synthesized through various techniques to produce CuF_2 electrodes that could be better utilized. CuF_2 electrodes were formed through sintering CuF_2 on metal current collectors or electrodeposition of CuF_2 thin films from HF solutions. Although a few of the techniques resulted in appreciable specific capacity, voltages were low, resulting in poor energy density. Questions remained regarding the dissolution of CuF_2, the formation of complex oxide-based reactions at lower voltages, and the recurring problem of very poor intrinsic electronic conductivity brought about by the high-band-gap metal fluorides. Although much work was done in this time period, the theoretical utilization of the metal fluorides was never really approached unless a partial dissolution of the electrode was involved, thereby enhancing the kinetics.[14] In this case, the cell exhibited poor stability. At this point, the majority of the interest in this compound faded.

The poor utilization of most fluorides resides in the high electronic resistance of the material brought about by their intrinsically high band gaps. This paper describes a series of new material chemistries that enable the primary reaction to take place in anhydrous copper-fluoride-based materials. The initial challenge in enabling CuF_2 is similar to the other metal fluorides, the highly ionic Cu−F bond induces a high band gap and very poor electronic conductivity. As opposed to carbon utilized in the previously demonstrated metal fluorides,[2−4,6,7] the electrochemical activity of copper fluoride has been enabled through the use of mixed conducting matrices (MCM). Although the CuF_2 nanocomposites incorporating carbon matrices resulted in some improvement, exceeding beyond 50% of theoretical capacity was not possible without the use of the MCM approach, which enabled 98% of theoretical capacity.

The MCM approach focuses on effective transport of both ions and electrons to the metal fluoride nanodomain. As shown in Figure 1, the initial electronic charge is brought to the nanocomposite via the conductive black in the porous positive electrode along with lithium ions through the conductive electrolyte. For a nanocomposite concept to be utilized effectively, the electronic and ionic charge must be transported from the carbon and lithium ion electrolyte conductors through a highly conducting matrix that links all the nanodomains within the nanocomposite. We utilized a

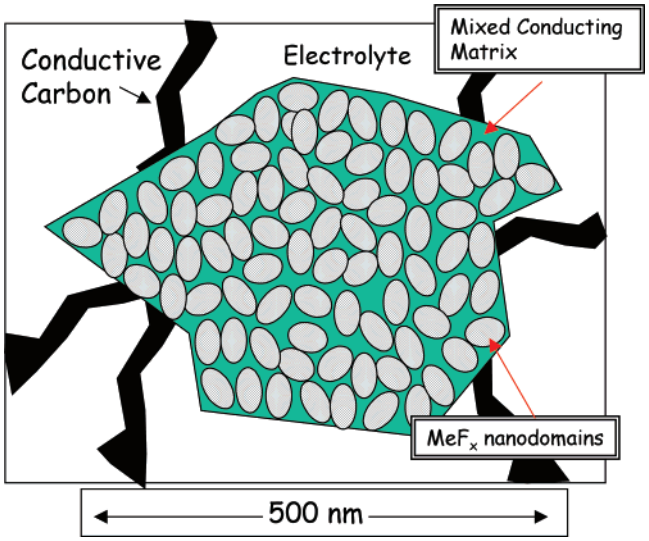

Figure 1. Schematic showing charge-transport issues relative to a metal fluoride nanocomposite containing a mixed conducting matrix.

mixed conducting matrix concept that combines the ionic and electronic transport duties into one material, the mixed conductor. Mixed conductors utilized as the matrix can be easily represented by intercalation compounds, which maintain excellent electronic and ionic conduction. To exhibit the latter, the material should intercalate and reduce at a voltage above or similar to the conversion reaction of the metal fluoride. Attractive materials such as V_2O_5, MoS_2, and $MoO_{3-\delta}$ can be utilized. Examples of metal fluorides enabled by these MCM matrices are nanocomposites of FeF_3 (V_2O_5),[2] BiF_3 (MoS_2),[15] and as discussed herein, CuF_2 (MoO_3). In all cases, the nanocomposites exhibit relatively low surface areas. This presumed detrimental effect is offset by the electronic and ionic charge being carried by the matrix to the individual nanodomains. The fabrication of a dense composite consisting of nanocrystallites (2−30 nm) of the metal fluoride embedded in a matrix of a mixed conducting compound results in the utilization of nanomaterial properties with lower liquid electrolyte interfacial area (reducing parasitic reactions), higher packing density, and possibly safety and processing advantages.

Within this paper, we demonstrate that the electrochemical activity of copper fluoride compositions can be enabled in the MCM approach by providing fast conductive pathways for both electrons and lithium through the mixed conducting oxide matrix. In addition, we present evidence that the synthesis of these highly conductive nanocomposites resulted in limited anion exchange or abstraction from the CuF_2 to the MoO_3 matrix.

2. Experimental Section

2.1. Nanocomposite Fabrication. Nanocomposites were fabricated by the introduction of approximately 1 g of copper fluoride into a high-energy milling cell along with approximately 5−50 wt

(12) Elliott, W. E.; Huff, J. R.; Simmons, G. L.; McDonald, G. D.; Jamrozy, J. L.; Towle, W. L. *A Program to Develop a High-Energy-Density Primary Battery With a Minimum of 200 Watt Hours Per Pound OF Total Battery Weight*; Contract Report NASA CR-54873; National Aeronautics and Space Administration: Washington, D.C., 1965.

(13) Abens, S. G.; Mahy, T. X.; Merz, W. C. *Development of High-Energy-Density Primary Batteries*; Contract Report NASA CR-54859; National Aeronautics and Space Administration: Washington, D.C., 1965.

(14) Farrar, J.; Keller, R.; Mazac, C. J. *Proceedings of the 18th Annual Power Sources Conference*, May 19−21, 1964, Fort Monmouth, NJ; PSC Publications: Ann Arbor, MI, 194; pp 92−94.

(15) Badway, F.; Mansour, A.; Plitz, I.; Pereira, N.; Weinstein, L.; Yourey, W.; Amatucci, G. G. Enabling Aspects of Metal Halide Nanocomposites for Reversible Energy Storage. In *Solid-State Ionics*; Traversa, E., Armstrong, T., Masquelier, C., Sadaoka, S., Eds.; Materials Research Society Symposium Proceedings 972; Materials Research Society: Warrendale, PA, 2007.

Table 1. Lattice Parameters and Primary Crystallite Size Derived from XRD for a Variety of CuF_2 Materials; Arrows are a Guide to the Relative Change in Parameter of the Oxide Matrix Nanocomposites vs the Carbon Matrix Materials.

sample	Cell V (Å^3)	lattice parameters (Å)			β angle (deg)	CuF_2 size on basis of (011) peak (nm)
		a	b	c		
CuF_2	68.70	3.294 ± 0.001	4.559 ± 0.002	4.606 ± 0.002	83.30 ± 0.03	58
CuF_2 + 15% C milled, no anneal	68.46	3.290 ± 0.002	4.557 ± 0.004	4.596 ± 0.003	83.42 ± 0.05	27
CuF_2 + 15% C 20 min 250 °C He	68.43	3.298 ± 0.002	4.547 ± 0.003	4.593 ± 0.003	83.40 ± 0.04	59
CuF_2 + 15% C 45 min 250 °C He	68.65	3.303 ± 0.001	4.551 ± 0.003	4.597 ± 0.002	83.41 ± 0.04	148
CuF_2 +15% C 20 min 200 °C He	68.72	3.301 ± 0.002	4.557 ± 0.004	4.599 ± 0.003	83.34 ± 0.05	44
CuF_2 + 7% MoO_3 20 min 200 °C He	68.92↑	3.290 ± 0.001↓	4.569 ± 0.002↑	4.615 ± 0.001↑	83.59 ± 0.02↑	21
CuF_2 + 15% VO_2 20 min 200 °C He	68.86↑	3.288 ± 0.003↓	4.562 ± 0.005↑	4.618 ± 0.004↑	83.71 ± 0.06↑	16
CuF_2 + 7% V_2O_5 20 min 200 °C He	68.83↑	3.292 ± 0.001↓	4.568 ± 0.003↑	4.605 ± 0.002	83.68 ± 0.04↑	21
CuF_2 + 15% NiO 20 min 200 °C He	68.89↑	3.293 ± 0.004↓	4.571 ± 0.005↑	4.607 ± 0.004↑	83.54 ± 0.06↑	15
CuF_2 + 7% CuO 1 h 200 °C He	69.06↑	3.295 ± 0.002	4.567 ± 0.003↑	4.620 ± 0.003↑	83.44 ± 0.05↑	16

Table 2. Comparison of Lattice Parameters for Various CuF_2 Materials and CuF_6 Octahedron Dimensions as Calculated from XRD Data

	CuF_2 macro	CuF_2 15% C	CuF_2 7% MoO_3
	Lattice Parameters		
a (Å)	3.29(4)	3.30(1)	3.29(0)
b (Å)	4.55(9)	4.55(7)	4.56(9)
c (Å)	4.60(6)	4.59(9)	4.61(5)
β (Å)	83.30	83.34	83.59
V (Å^3)	68.70	68.72	68.92
	Cu−F Bond Length		
planar 1	1.911	1.910	1.915
planar 2	1.928	1.930	1.932
axial 1	2.301	2.303	2.297

% conductive matrix. The as-received CuF_2 (Aldrich) was anhydrous and verified through the use of XRD and FTIR. In later experiments outside the scope of this paper, commercial batches were obtained that were not completely anhydrous; these were purified by either HF or NH_4F treatments with some difficulty. The cell was sealed under helium and high-energy milled (HEM) for various times in a Spex 8000 milling apparatus. Afterward, the cell was opened and the contents were removed in the helium atmosphere of the glove box.

2.2. Electrochemical Characterization. Electrodes were prepared by adding poly(vinylidene fluoride-co-hexafluoropropylene) (Kynar 2801, Elf Atochem), carbon black (Super P, MMM), and dibutyl phthalate (DBP) (Aldrich) to the active materials in acetone. The slurry was tape-cast, dried for 1 h at 22 °C, and rinsed in 99.8% anhydrous ether (Aldrich) to extract the DBP plasticizer. The electrodes, 1.25 cm^2 disks typically containing 57 ± 1% active material and 13 ± 1% carbon and 30% Kynar 2801, were tested electrochemically versus Li metal (FMC). The Swagelock (in-house) or coin (NRC or Hohsen) cells were assembled in a He-filled dry box using Whatman GF/D glass fiber separators saturated with 1M $LiPF_6$ in 1:1 vol/vol ethylene carbonate:dimethyl carbonate electrolyte (Ferro). The cells were controlled by Mac-Pile (Biologic) or Maccor battery cycling systems. Cells were cycled under a constant current of 7.58 mA g^{-1} of composite at 24 °C, unless noted otherwise.

2.3. Physical Characterization. *(a) X-ray Diffraction.* The as-fabricated and annealed materials structures were identified by ex situ X-ray diffraction (XRD) using silicon (−325 mesh powder, Johnson Matthey) as internal standard in a X2 Scintag diffractometer with Cu Kα as radiation source at a 0.2°/min scan rate. A least-square fit determined a coefficient for a second-order polynomial used to correct all the observed peaks of the spectrum before lattice parameter calculation.

(b) Transmission Electron Microscopy. The material microstructure was analyzed by combined transmission electron microscopy (TEM) and selected area electron diffraction (SAED) using a Topcon 002B microscope operating at 200 kV. The samples were prepared by dispersing the powder in dimethyl carbonate and releasing a few drops of the liquid on a "lacey" carbon film supported on a copper mesh grid. The TEM sample preparation was done in a He-filled glovebox and the samples were sealed in a He-filled pouch. Sample transfer to the TEM was done in air with less than 30 s air exposure. In addition to bright and tilted dark-field imaging, selected area electron diffraction patterns (SAED) from various areas were obtained to determine the structure of the phases present. The tilted dark-field images were obtained by centering the aperture on part of the most intense (011) ring of CuF_2. Moreover, grain size distribution was obtained by first processing the dark-field images according to Image Processing Handbook,[16] followed by quantification of binary images.

(c) X-ray Absorption Spectroscopy. The X-ray absorption spectroscopy (XAS) experiments were conducted on the bending magnet station X-11A of the National Synchrotron Light Source with the electron storage ring operating at an electron energy of 2.8 GeV and a stored current in the range of 200−300 mA.[17] X-ray absorption fine structure (XAFS) spectra were collected in the transmission mode at room temperature with a variable exit double-crystal monochromator using two flat Si(111) crystals. The energy resolutions at the Cu and Mo K-edges were estimated to be 2.5 and 10.3 eV, respectively, compared to the Cu and Mo core hole natural line widths[18] of 1.55 and 4.55 eV, respectively. The harmonic-content of the beam was minimized by controlling the parallelism of the monochromator crystals to reduce the beam intensity by 20% for both the Cu and Mo K-edge spectra. The incident and transmitted X-ray intensities were monitored using ionization chambers. For the Cu K-edge spectra, about 25 and 60% of the incident and transmitted X-rays, respectively, were absorbed with an appropriate mixture of nitrogen and argon flowing through the ionization chambers. For the Mo K-edge spectra, about 20 and 35% of the incident and transmitted X-rays, respectively, were absorbed with only Ar flowing through the ionization chambers. The energy calibration of the monochromator was monitored using a 5 μm thick Cu foil and a 15 μm thick Mo foil placed between the transmitted beam chamber and a third ionization chamber having the same fill gas as the transmitted beam chamber.

For the XAS experiments, the powders were sifted through a 20 μm mesh sieve and thoroughly mixed with boron nitride and pressed into self-supporting pellets with a relatively uniform thickness. The X-ray absorption edge jumps for the oxide and foil samples were kept below 1.5 in order to minimize the effects of pinholes and particle size on XAFS amplitudes.[19,20]

(16) Russ, J. C. *The Image Processing Handbook*, 5th ed.; CRC Press: Boca Raton, FL, 2007.
(17) Sayers, D. E.; Heald, S. M.; Pick, M. A.; Budnick, J. I.; Stern, E. A.; Wong, J. *Nucl. Instrum. Methods Phys. Res.* **1983**, *208*, 631.
(18) Krause, M. O.; Oliver, J. H. *J. Phys. Chem. Ref. Data* **1979**, *8* (2), 329.
(19) Lu, K. Q.; Stern, E. A. *Nucl. Instrum. Method* **1983** *212*, 475.
(20) Stern, E. A.; Kim, K. *Phys. Rev. B* **1981**, *23*, 3781.

Table 3. Summary of Quantitative Analysis of the EXAFS Spectra for Cu, CuF_2, and the Nanocomposite of CuF_2

	sample							
	CuF_2	CuF_2	CuF_2 (NC)	CuF_2 (NC)	CuF_2 (NC)	CuF_2 (NC)	Cu	Cu
$k_{min} - k_{max}$ (Å^{-1})	3.0−12.8	3.0−12.8	3.0−12.8	3.0−12.8	3.0−12.8	3.0−12.8	3.0−12.0	3.0−12.0
$R_{min} - R_{max}$ (Å)	0.85−2.18	1.22−2.18	0.85−2.18	1.22−2.18	0.85−2.18	1.22−2.18	1.41−3.07	1.81−2.73
N_1	4	4	4	4	4	4	12	12
R_1 (Å)	1.95 ± 0.01	1.95 ± 0.01	1.95 ± 0.01	1.95 ± 0.01	1.95 ± 0.01	1.95 ± 0.01	2.552 ± 0.005	2.551 ± 0.005
$1 \times 10^3 \sigma_1^2$ (Å^2)	5.4 ± 0.9	5.4 ± 0.8	3.9 ± 1.5	3.8 ± 1.1	5.3 ± 0.6	5.4 ± 0.5	8.9 ± 0.6	8.9 ± 0.6
N_2	2	2	2	2	2	2		
R_2 (Å)	**2.30 ± 0.05**	2.30 ± 0.04	2.22 ± 0.16	2.23 ± 0.14	2.26 ± 0.05	2.26 ± 0.05		
$1 \times 10^3 \sigma_2^2$ (Å^2)	19.9 ± 7.4	19.6 ± 6.2	30.6 ± 42.3	32.3 ± 34.5	18.2 ± 8.1	17.7 ± 6.8		
E_0 (eV)	3.6 ± 1.9	3.6 ± .9	4.1 ± 3.2	4.5 ± 2.6	3.9 ± 2.7	4.0 ± 2.8		
S_0^2	0.82 ± 0.10	0.81 ± 0.09	0.65 ± 0.17	0.63 ± 0.12	0.82	0.82	0.99 ± 0.09	0.99 ± 0.09
R-factor	0.0081	0.0027	0.019	0.0049	0.0235	0.0112	0.0086	0.0044
red. chi-square	392	285	638	343	632	522	801	1002

(d) X-ray Absorption Spectroscopy Data Analysis. The X-ray absorption spectra were calibrated with respect to the first inflection point energy of the K-edges of metallic Cu and Mo at 8979 and 19 999 eV, respectively. The K-edge absorption was isolated by fitting the pre-edge region (−300 to −30 eV for the Cu K-edge and −300 to −100 eV for the Mo K-edge, relative to the inflection point energy) with the Victoreen formula, extrapolating over the entire range of the spectrum and subtracting the background from the entire spectrum. Energy-independent step normalization was applied by dividing the absorption cross-section with the value of the average absorption in the range100−400 eV above the edge energy. The extended X-ray absorption fine structure (EXAFS), χ(k), was extracted using multinode cubic spline procedures, which minimized the amplitude of nonphysical peaks in the 0−0.9 Å region of the Fourier transform.[21,22] The data analysis up to this point was carried out using the WinXAS software package (version 3.1).[23,24]

All fits were made using the curve fitting code FEFFIT of the UWXAFS software package.[25] The data were fitted using theoretical standards calculated on the basis of the curved-wave scattering formalism of the FEFF Code (version 8.2).[26,27] The FEFF calculations were performed using established structural models for Cu[28] and CuF_2[29] standards. The Fourier transforms were generated using k^3-weighted EXAFS spectra over the $k_{min} - k_{max}$ ranges listed in Table 3 with a Hanning window of 1.0 Å^{-1}. The fits were performed in real space over the $R_{min} - R_{max}$ ranges, which are also listed in Table 3. In fitting the data, the many body amplitude reduction factor (S_0^2) or coordination number (N), coordination distance (R), and disorder (σ^2) were used as floating parameters. One inner potential (E_0) was used in the analysis of multiple shell fits and a Gaussian disorder was assumed for all shells. The number of fitting parameters was kept below the maximum number of independent data points allowed by the Brillouin theorem.[30] The goodness of each model was monitored by the value of the reduced Chi square defined as the sum of the squares of the difference between measured and model data normalized to the number of degrees of freedom in the fit. The number of degrees of freedom is given as the difference between the number of independent data points and the number of floating parameters. Another measure of the goodness of each model is given by the value of the *R*-factor, which is the sum of the square of residuals between measured and model data normalized to the magnitude of the measured data.

3. Results and Discussion

3.1. CuF_2:Carbon Nanocomposites. *(a) Structure.* Carbon metal fluoride nanocomposites (CMFNCs) were initially prepared through the previously optimized method of high-energy milling with 15% carbon.[2−4,6,7] Numerous synthesis parameters were investigated, including milling time and postannealing at a range of temperatures in a He atmosphere to restore a small degree of crystallinity to the nanocomposite. The resultant XRD patterns of the CuF_2:C nanocomposites are shown in Figure 2. Peak breadth, indicative of the nanocomposite nature of the material, varies as a function of fabrication parameters and resulting nanocomposite size. On the basis of the Scherrer formula, the broadness was consistent with a nanocrystallite size ranging from 27 to 148 nm, as shown for a number of representative samples in Table 1. We have previously shown that the Scherrer formula was consistent with Williamson Hall and HRTEM in determining the primary crystallite size of metal fluoride nanocomposites, even when prepared under strain-inducing high-energy techniques.[7] For samples that were HEM for long periods of time or higher temperatures, small Bragg reflections related to Cu metal were observed to grow. Note that all the C matrix composite lattice parameters are consistent with the lattice parameters of native CuF_2, as shown quantitatively in Table 1; therefore, no intrinsic change to the CuF_2 crystal besides size was identified. The Bragg peak quartet between 54 and 58° 2θ is a good qualitative visual indicator of the rutile structure's monoclinic distortion primarily due to the presence of the (200) and (022) reflections and will be utilized throughout this paper.

(b) Electrochemistry. The CuF_2:C nanocomposites were characterized for their first discharge specific capacities in 1 M $LiPF_6$ EC:DMC from OCV to 2.5 V. The results are shown in Figure 3; also included is a macrocomposite of CuF_2:15% C as a benchmark reference. The use of CMFNC clearly resulted in a significant increase (150%) in discharge

(21) Sayers, D. E.; Bunker, B. A. *X-ray Absorption: Principles, Applications, Techniques of EXAFS, SEXAFS and XANES*; Koningsberger, D. C., Prins, R., Eds.; Wiley: New York, 1988; Chapter 6.
(22) Cook, J. W., Jr.; Sayers, D. E. *J. Appl. Phys.***1981**, *52*, 5024.
(23) Ressler, T. *J. Synchrotron Radiat.* **2000**, *5*, 118.
(24) Ressler, T. *J. Phys. IV* **1997**, *7*, C2−269.
(25) Stern, E. A.; Newville, M.; Ravel, B.; Yacoby, Y.; Haskel, D. *Physica B* **1995**, *208−209*, 117.
(26) Ankuudinov, A. L.; Ravel, B.; Rehr, J. J.; Conradson, S. D. *Phys. Rev. B* **1998**, *58*, 7565.
(27) Ankudinov, A. L.; Boulden, C. E.; Rehr, J. J.; Sims, J.; Hung, H. *Phys. Rev. B* **2002**, *65*, 104107.
(28) Vilars, P.; Calver, L. D. *Pearson's Handbook of Crystallographic Data for Intermetallic Phases*; American Society for Metals: Metals Park, OH,1985; Vol. 3, p 1023.
(29) Fischer, P.; Halg, W.; Schwarzenbach, D.; Gamsjager, H. *J. Phys. Chem. Solids* **1974**, *35*, 1683.
(30) Stern, E. A. *Phys. Rev. B* **1993**, *48*, 9825.
(31) Yokoyama, T.; Satsukawa, T.; Ohta, T. *Jpn. J. Appl. Phys.* **1989**, *28* (10), 1905.

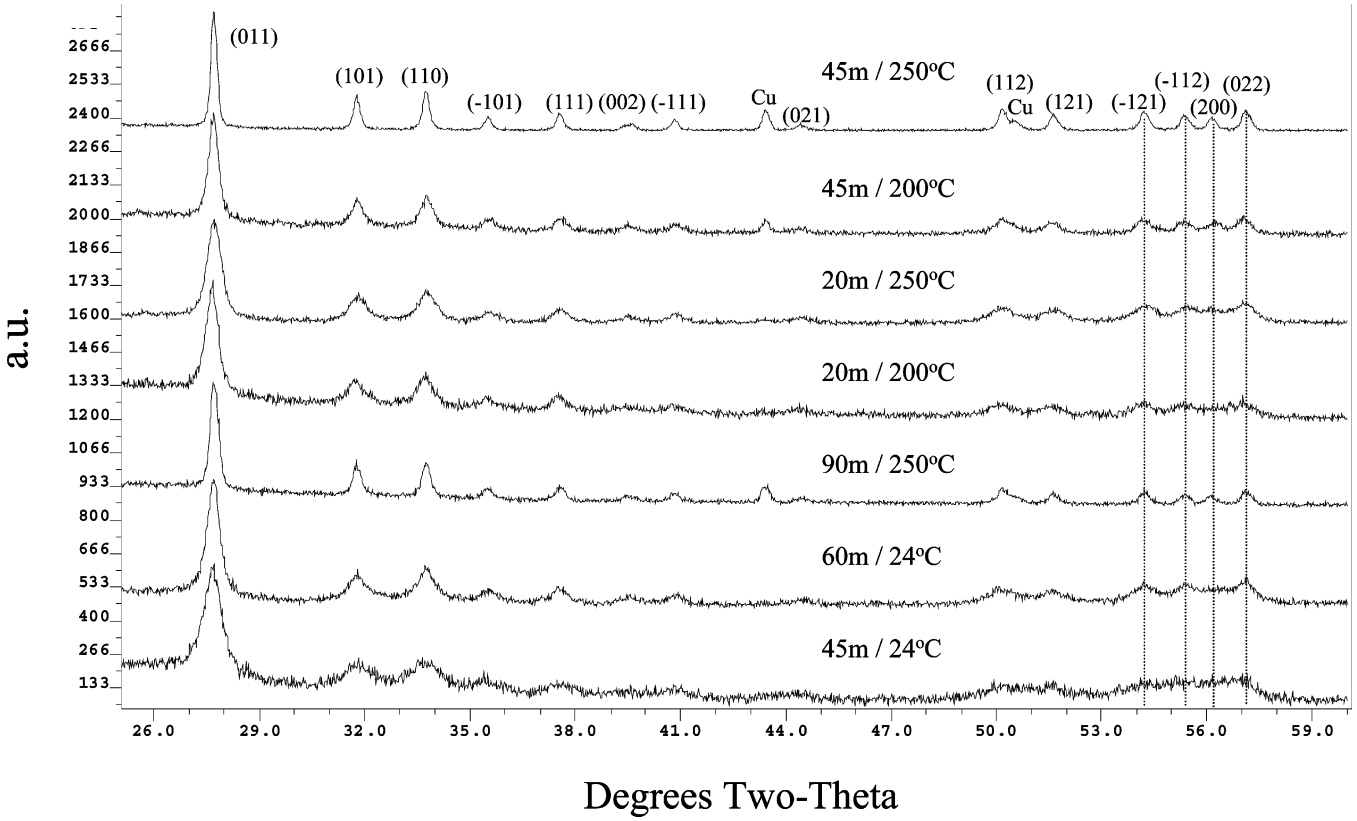

Figure 2. XRD patterns of 15 wt % C:85 wt % CuF_2 nanocomposites of various synthesis conditions. Labels indicate high-energy milling time (m = min) and post fabrication annealing temperature. All annealing was performed for 5 h under He.

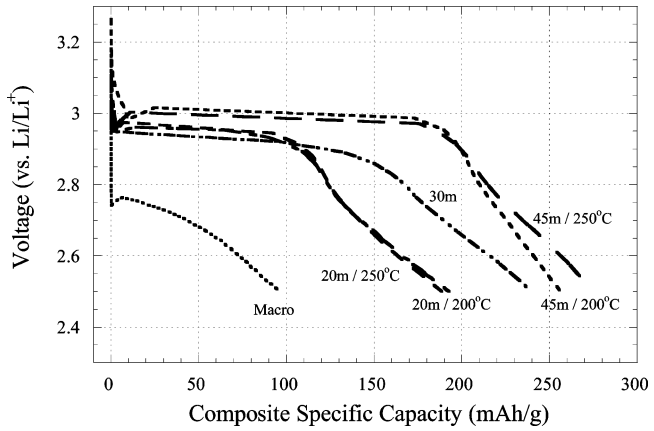

Figure 3. Voltage profiles for 15% C:85% CuF_2 CMFNC nanocomposites of various synthesis parameters. Labels indicate high-energy milling time (m = min) and postfabrication annealing temperature. All annealing performed for 5 h under He. Macro-CuF_2 mixed thoroughly with 15% carbon is included as reference.

capacity relative to the CuF_2:15%C macrocomposite because of the nanocomposite effect on ionic and electronic transfer. However, the specific capacity of 250 mA h g^{-1} was well short of the theoretical specific capacity of 528 mA h $g^{-1}$for CuF_2 or 448 mAh g^{-1} expected for a 15% carbon nanocomposite. The basis for the poor specific capacity utilization may be related to a perceived tendency for a reduction reaction during synthesis

$$CuF_2 + C \rightarrow CuF_{2-z} + CF_x$$

However, we have not seen overt evidence of CF_x formation (via XRD, SAED, or FTIR techniques). The lack of ability of C to reduce CuF_2 is consistent with the redox potentials of the respective oxidation and reduction reactions. The theoretical redox based on $Cu^{2+}F_2$ is approximately 3.55 V vs Li/Li^+, whereas the theoretical reduction potential of CF in solid-state reactions has been shown to be approximately 4.5 V on the basis of thermodynamic data.[8] Regardless of mechanism, evidence of some CuF_2 reduction can be found in the presence of small Bragg reflections related to Cu formation in Figure 2. However, linking the presence of Cu to poor performance is far from conclusive, as the percent of converted Cu (<10%) is not consistent with the degree of poor utilization measured and the performance of the samples did not inversely scale with the amount of Cu identified in XRD. In fact, the best performing carbon nanocomposite samples contained a small fraction of Cu, which most likely assisted the electrical conductivity. To further investigate the possibility of a solid-state redox effect, we reduced the reduction power of carbon by fabricating CuF_2 nanocomposites with carbon fluoride. A partially ionic CF_x of composition $CF_{0.8}$ was chosen as the matrix. These nanocomposites offered little improvement relative to the non-fluorinated carbons and had no evidence of CuF_2 dehalogenation, thereby further suggesting that the reduction mechanism is not the sole basis for the poor utilization.

3.2. CuF_2:Metal Oxide Mixed Conducting Nanocomposites. *(a) Structure.* A number of CuF_2 nanocomposites were fabricated utilizing a wide variety of metal oxides, including NiO, MoO_2, MoO_3, VO_2, V_2O_5, and CuO. Of these, MoO_2 ($P2_1/n$) is somewhat isostructural with the monoclinically distorted rutile ($P2_1/n$) CuF_2. As with the carbon matrix nanocomposites, the metal oxide matrix nanocomposites were

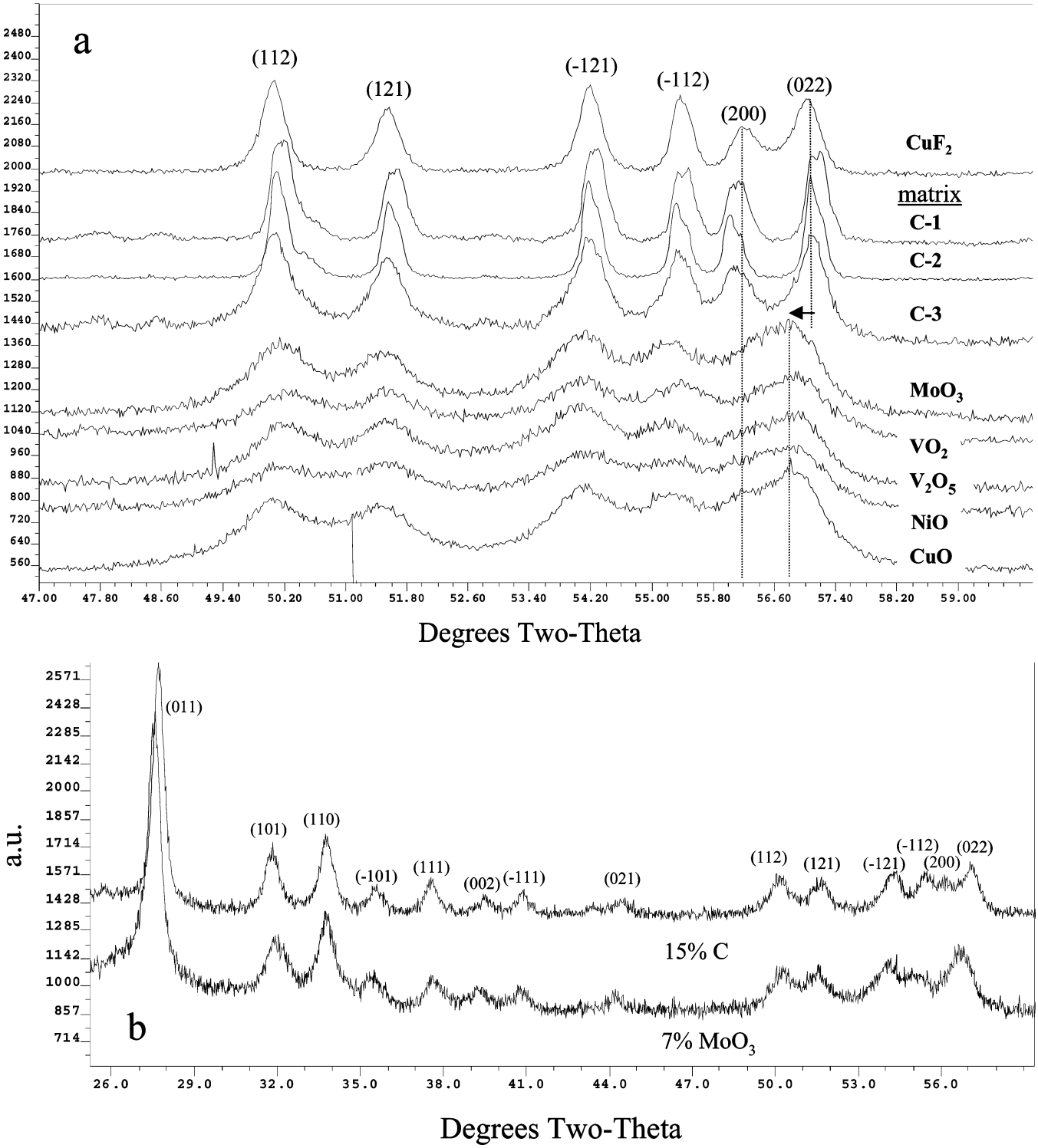

Figure 4. (a) Zoom of the XRD patterns of various nanocomposites vs the CuF_2 standard showing modification of the core CuF_2 structure occurring for all metal-oxide-based matrices. (b) XRD patterns showing contrast in full pattern of a CuF_2 15% C nanocomposite vs a CuF_2 7% MoO_3 nanocomposite leading to expansion of *b* and *c* parameters and increase in the β angle and volume of the monoclinic structure.

synthesized under various milling and postannealing conditions. XRD results of selective examples of MCM nanocomposites are shown in Figure 4. These patterns are representative of all samples, both annealed and unannealed, and their specific treatments are given in Table 1. All samples, regardless of the oxide matrix, resulted in broad reflections consistent with the formation of a nanocomposite with CuF_2 domains on the order of 15−21 nm. The peaks were broader than most of the C-based nanocomposites. It will be apparent from the following discussions that this may be due to a compositional nonuniformity as opposed to a distinct crystallite size difference. Of most interest is the distinct and consistent shift toward smaller angles of the (*0kl*) Bragg reflections such as (022) of the CuF_2 nanocomposites with metal oxide matrices relative to the C matrix CuF_2 nanocomposites included for comparison. This is very apparent in the comparison of the CuF_2 15% C nanocomposite vs the CuF_2 7% MoO_3 nanocomposite shown in Figure

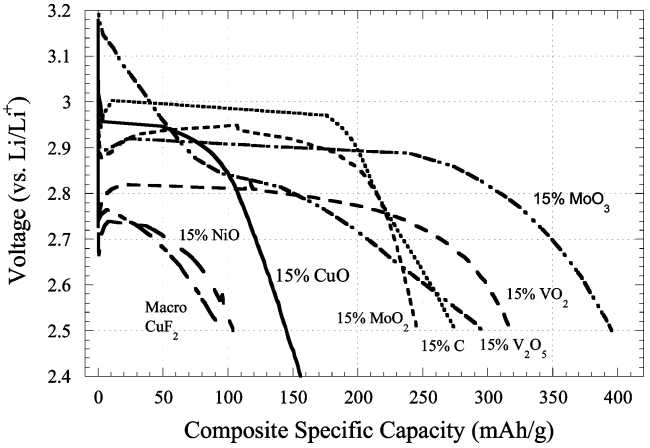

Figure 5. Comparison of the voltage profile vs specific capacity of all matrices. The best samples with respect to synthesis conditions for each matrix were utilized in this comparison.

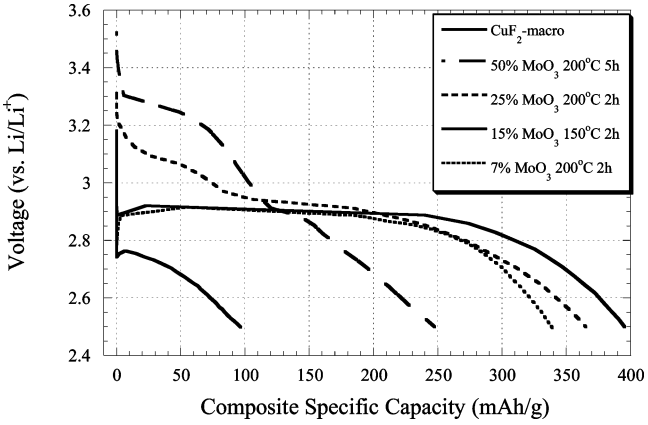

Figure 6. Voltage profile for optimized CuF_2 nanocomposites containing 0, 7, 15, 25, and 50% MoO_3. Samples were heat-treated in He as indicated in the legend; 7% nanocomposite was high-energy milled for 60 min and all others were milled for 20 min. The best heat treatment for each percentage was utilized.

4b. Indeed, all the CuF_2 materials formed with an oxide matrix material resulted in a significant lattice parameter change regardless of the cation utilized. The lattice parameters of the CuF_2 materials are shown in Table 1 for comparison. The inclusion of the oxide matrix results in an increase in the β angle (reduction of rutile monoclinic distortion) and volume, a very slight decrease in the *a* lattice parameter and a notable increase in the *b* and/or *c* lattice parameters relative to carbon-based nanocomposites and the macrostructured CuF_2 benchmark. Relative to the CuF_6 octahedron, the lattice parameter induces a slight increase in the planar Cu−F bonds length and decreases the axial bonds length. The results are summarized in Table 2 for a macrocrystalline standard CuF_2, a CuF_2−C nanocomposite, and a CuF_2−MoO_3 nanocomposite.

(b) Electrochemistry. Electrochemical results are summarized in the voltage comparisons of Figure 5 (the best of each matrix from this initial evaluation was chosen for this comparison). These are compared with macro CuF_2 and the best carbon-based nanocomposite. The best oxide matrices were found to be of the molybdates and vanadates. In contrast, matrices of NiO and CuO were found to result in much poorer performance. The basis for the very poor performance of compounds such as NiO and CuO can be traced to the fact that these are not true mixed conducting matrix materials. Although CuO exhibits excellent electrical conductivity, neither NiO or CuO have the propensity for lithium intercalation, which would lead to excellent ionic conductivity. At sufficiently low voltages, these compounds convert to the base metal and Li_2O, a composite with relatively low ionic conductivity. Regardless, such conversion potentials are well below the activity range of CuF_2 and are never reached in our studies here. This is in sharp contrast to the intercalation potentials of VO_2, V_2O_5, and MoO_3, whose insertion reactions are in the range of the actual conversion potentials of CuF_2 and can be intercalated to give excellent ionic conductivity before and during the conversion process. Because the excellent electrochemical activity of the CuF_2 nanocomposites utilizing a MoO_3 MCM (400 mA h g^{-1}, vs approximately 250 mA h g^{-1} for carbon nanocomposite matrix compared to 100 mA h g^{-1} for macrostructured CuF_2), these compositions were studied in more detail as a model system for the MCM approach utilizing oxides.

3.3. CuF_2 Molybdate Nanocomposites. *(a) Electrochemistry.* Various MCM nanocomposites were fabricated with 50, 25, 15, and 7% MoO_3. The nanocomposites were postannealed under various inert atmosphere, time, and temperature conditions. The better representative voltage profiles and heat treatment of each percentage are shown in Figure 6. The high 50% MoO_3 materials revealed two pseudoplateaus; the lower voltage region is associated with the CuF_2 conversion reaction and the higher voltage region is not defined but is consistent with unpublished results and theoretical calculations of a $Cu^{2+} \rightarrow Cu^{1+}$ transition. Lower percentages of MCM show more of a uniform conversion profile consistent with that of CuF_2. When optimized with 7% MoO_3 and milled in ZrO_2 lined cells, the specific discharge capacity was measured to be as high as 450 mA h g^{-1} on the basis of the weight of the entire nanocomposite when cycled to 2 V (Figure 10 and Figure 14). When corrected for the weight of the oxide matrix, the nanocomposite has exhibited 525 mA h g^{-1}, corresponding to 99% of the theoretical capacity of CuF_2.

(b) Structure. As discussed above, a distinct increase in the *b* and/or *c* lattice parameter, and very slight shrinkage of the *a* lattice parameter of monoclinic CuF_2 has been identified for all nanocomposites utilizing oxide matrices when compared with CuF_2 or C:CuF_2 nanocomposites (Table 1). The electronic and structural modification was examined in more detail through ex situ X-ray absorption spectroscopy (XANES and EXAFS).

XANES. A comparison of the Cu K-edge XANES data for the CuF_2:15% MoO_3 nanocomposite along with Cu, $Cu^{1+}{}_2O$, $Cu^{2+}O$, and $Cu^{2+}F_2$ reference compounds is shown in Figure 7a. In Figure 7b, we show the comparison of the first derivative of normalized XANES data for the CuF_2: 15% MoO_3 nanocomposite and the CuF_2 standard. The reference spectra of the Cu foil that was measured during the CuF_2:15% MoO_3 nanocomposite and the CuF_2 standard runs are displayed in Figure 7c. The two sets of reference spectra are identical, confirming the exceptional accuracy of the energy calibration scheme. The Cu K-edge spectra of

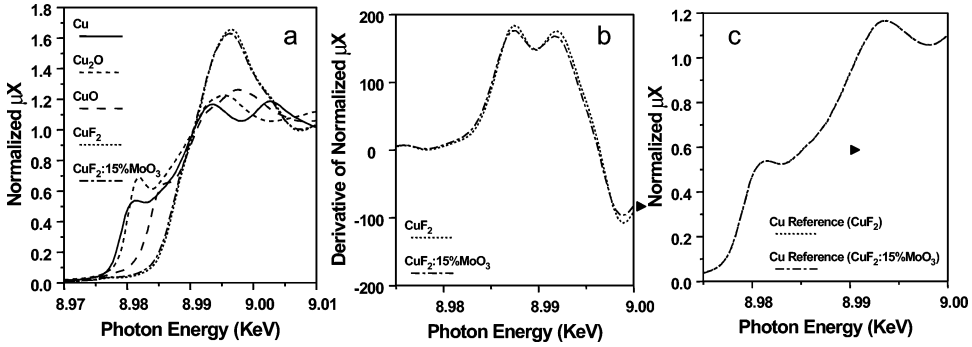

Figure 7. (a) XANES spectra comparing Cu in CuF_2:15% MoO_3 matrices vs that of CuF_2 and Cu^{1+}- and Cu^{2+}-containing oxide standards, (b) derivative of normalized XANES for CuF_2 and CuF_2:15% MoO_3, (c) XANES of the reference Cu foil collected simultaneously with CuF_2 and the CuF_2 nanocomposite indicating that any small shift observed in the measured spectra is real.

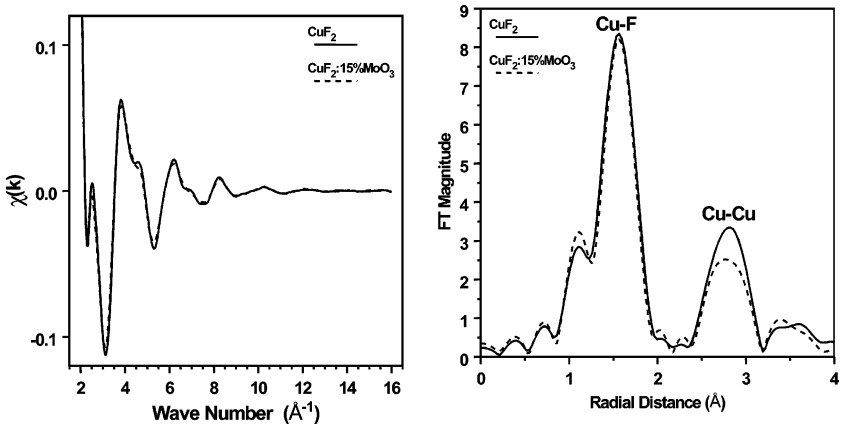

Figure 8. EXAFS spectra (left) and their phase-uncorrected Fourier transform of CuF_2:15% MoO_3 nanocomposite compared with that of the CuF_2 standard. (FT range 3.0−12.8 $Å^{-1}$, k^3-weighted, and Hanning window of 1.0 $Å^{-1}$).

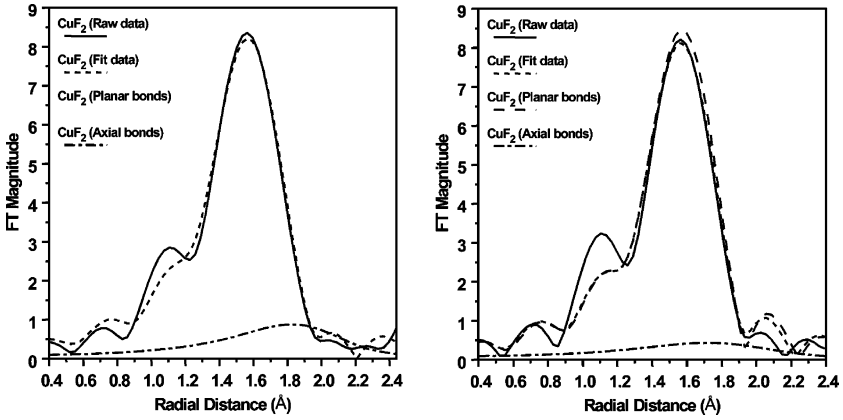

Figure 9. Comparison between raw and fit data as well as the individual contributions from the 4 square planar Cu−F bonds and the 2 axial Cu−F bonds for the CuF_2 standard (left) and the CuF_2:15%MoO_3 nanocomposite (right). (FT range is 3.0−12.8 $Å^{-1}$, k^3-weighted, and Hanning window of 1.0 $Å^{-1}$).

the various reference compounds in Figure 7a display a positive energy shift with an increase in formal valency. The energy at half-height for CuO is shifted by 3.9 eV, whereas that for the CuF_2 standard is shifted by 7.1 eV relative to metallic copper. In both cases, the Cu^{2+} ions have a distorted octahedral coordination. The higher energy shift for CuF_2 is attributed to the higher electronegativity of fluorine relative to oxygen. The Cu−F bonds are ionic in character, whereas the Cu−O bonds are covalent in character, leading to a decrease in the electron density of copper in CuF_2 and thus, a higher effective oxidation state. The Cu K-edge energy at half-height for the CuF_2:15% MoO_3 nanocomposite is shifted by 6.9 eV relative to copper. The edge shifts for the CuF_2: 15% MoO_3 and the CuF_2 standard are similar within the uncertainty of ± 0.2 eV normally quoted for the edge data. However, the exceptional match of the reference spectra presented in Figure 7c points to a much greater degree of certainty in the edge energy. Hence, the edge shift for the nanocomposite of −0.2 eV relative to the CuF_2 standard may likely be significant, suggesting a slightly lower effective oxidation state. A lower effective oxidation state can arise from anion abstraction from CuF_2 to MoO_3 or an anion exchange with excessive vacancy formation on the anion sublattice. A comparison of the derivative spectra for the CuF_2:15% MoO_3 and the CuF_2 standard (Figure 7b) shows slight broadening and shift in the XANES features for the nanocomposite relative to the CuF_2 standard, which could also be due to this mechanism. If one assumes that the

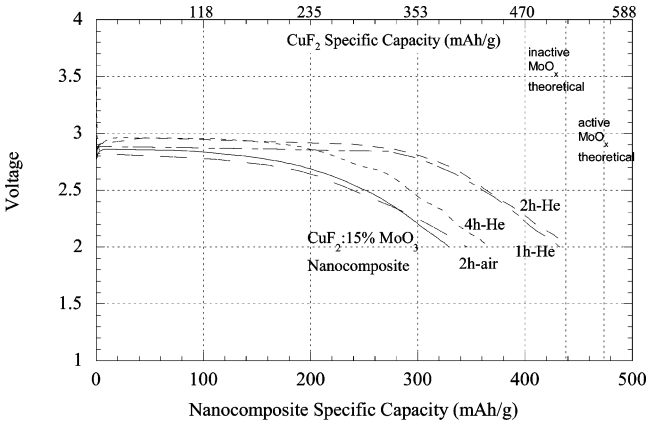

Figure 10. Electrochemical performance of CuF_2 MoO_3 nanocomposites fabricated in ZrO_2-lined cells. Dotted lines indicate theoretical performance in the case of MoO_3 being electrochemically active or not. Times indicate time of annealing at 250 °C. Specific capacity is given on the basis of the entire nanocomposite weight (lower) or CuF_2 (upper).

reduction in the edge energy of the nanocomposite relative to the CuF_2 standard is due to the anion abstraction, then the degree of Cu^{2+} reduction is roughly estimated to be 3% (as given by $100 \times (7.1-6.9/7.1)$) leading to the formation of $CuF_{1.94}$. However, if it is due to a nonstoichiometric anion exchange, as in $CuF_{2-z-x}O_zV_{(F)x}$ (V = vacancy), the degree of anion exchange can be up to a few percent (the limit to where the exchange would be noticeable by EXAFS) as long as the average oxidation state remains 1.94.

EXAFS. To further illustrate the structure of the nanocomposite, in Figure 8 we show the Cu K-edge EXAFS spectra and the corresponding Fourier transforms for the CuF_2:15% MoO_3 nanocomposite and the CuF_2 standard. The Fourier transform for the CuF_2 nanocomposite is similar to that of the CuF_2 standard. The Fourier transforms display two major peaks. One peak is due to contributions from the distorted CuF_6 octahedron and a second peak due to a contribution from the second shell of Cu−Cu. The small reduction in the amplitude of the Cu−Cu contribution for the nanocomposite can be due to structural disorder introduced by anion abstraction from CuF_2 to MoO_3 or anion exchange.

The local structure parameters for Cu, CuF_2 standard, and the CuF_2:15% MoO_3 nanocomposite are summarized in Table 3. A single-shell fit was used to analyze the first coordination sphere of Cu. In this fit, the coordination number (N_1) was constrained to the crystallographic value of 12 and S_0^2 was used as a floating parameter. Quantitative results for metallic Cu reveal a first shell distance of 2.552 Å and a disorder of 8.9×10^{-3} Å^2, in agreement with well-established results. These results provided a reliability check to our data collection and quantitative analysis procedures.

For CuF_2 and its nanocomposite, the first coordination sphere was analyzed in terms of two contributions to account for the distorted coordination of the CuF_6 octahedron. One contribution is due to four Cu−F bonds in an approximate square planar arrangement and a second one is due to two Cu−F axial bonds. Again, the coordination numbers (N_1 and N_2) were constrained to 4 and 2, whereas S_0^2 was used as a floating parameter. As can be seen from Table 3, within the uncertainty in the data, the value of S_0^2 for the nanocomposite is similar to that for the CuF_2 standard. Therefore, the data for the CuF_2:15% MoO_3 nanocomposite was also analyzed using the value of S_0^2 obtained for the CuF_2 standard, because it has a lower degree of uncertainty. Fourier transforms of the experimental spectra and simulated spectra as well as individual contributions from planar and axial bonds are shown in Figure 9.

For the CuF_2 standard, the Cu−F square planar distance of 1.95 ± 0.01 Å is slightly larger than 1.93 Å, which is the average of two distances derived on the basis of neutron diffraction data. The Cu−F axial distance of 2.30 ± 0.05 Å for the CuF_2 standard is in agreement with the value derived on the basis of neutron diffraction data of 2.31 Å. It is to be noted that the axial bonds contribution is significantly smaller than the square planar bonds contribution because of a significantly higher disorder in the case of the axial bonds (0.0196 compared to 0.0054 Å^2). The quality of the fit as measured by the value of the R-factor is significantly better in the case of the CuF_2 standard. When the value of S_0^2 for the nanocomposite was constrained to that for the CuF_2 standard, the uncertainties in the parameters for the axial bonds were significantly reduced. In all, the axial bond distance of the CuF_2 nanocomposite (2.22−2.26) was reduced relative to the CuF_2 standard (2.30), despite overlap in statistical significance. This is consistent with the octahedron bond decrease identified in the nanocomposite by XRD (Table 2). The overall poorer quality of the fit in the case of the nanocomposite could be due to some distortions in local structure as a result of anion exchange or fluorine abstraction that are not accounted for in the fitting model.

It is to be noted that coordination distances with a separation δR less than the value of $\pi/2k_{max}$ cannot be resolved from each other; k_{max} is the maximum of the photoelectron wave number used to fit the data. For a k_{max} of 12.8 Å^{-1}, δR is estimated to be 0.12 Å. Therefore, the splitting of the square planar arrangement of the Cu−F bonds into 2 Cu−F bonds at 1.917 Å and 2 Cu−F bonds at 1.936 Å cannot be resolved by XAS and should be treated as a single shell of 4 Cu−F bonds with an average distance at 1.926 Å, as we have done here. The 2 Cu−F axial bonds with a distance at 2.310 Å is resolvable from the average distance of the square planar bonds. It is also to be noted that a distribution of distances in close proximity of each other introduces structural disorder, which can be easily recognized by examining the disorder for the Cu−F shell.

(c) CuF_2 Matrix Nanocomposite Reaction. As discussed earlier, a significant structural change to the CuF_2 lattice was not observed in any of the carbon-based nanocomposites even when a wide variety of parameters were utilized for fabrication or posttreatment. This points to an innate effect of the oxide matrices to the observed distortion in the crystal lattice of CuF_2. Cation or anion exchange from the metal oxides to the copper fluoride is a distinct possibility, as is fluorine extraction. Cation exchange can be ruled out with the use of CuO as the matrix oxide. From Figure 4 and Table 1, it is clear that CuO induces the crystallographic change to the CuF_2 similar if not more so than other metal oxides. As both the CuO matrix and the CuF_2 consist of identical cations,

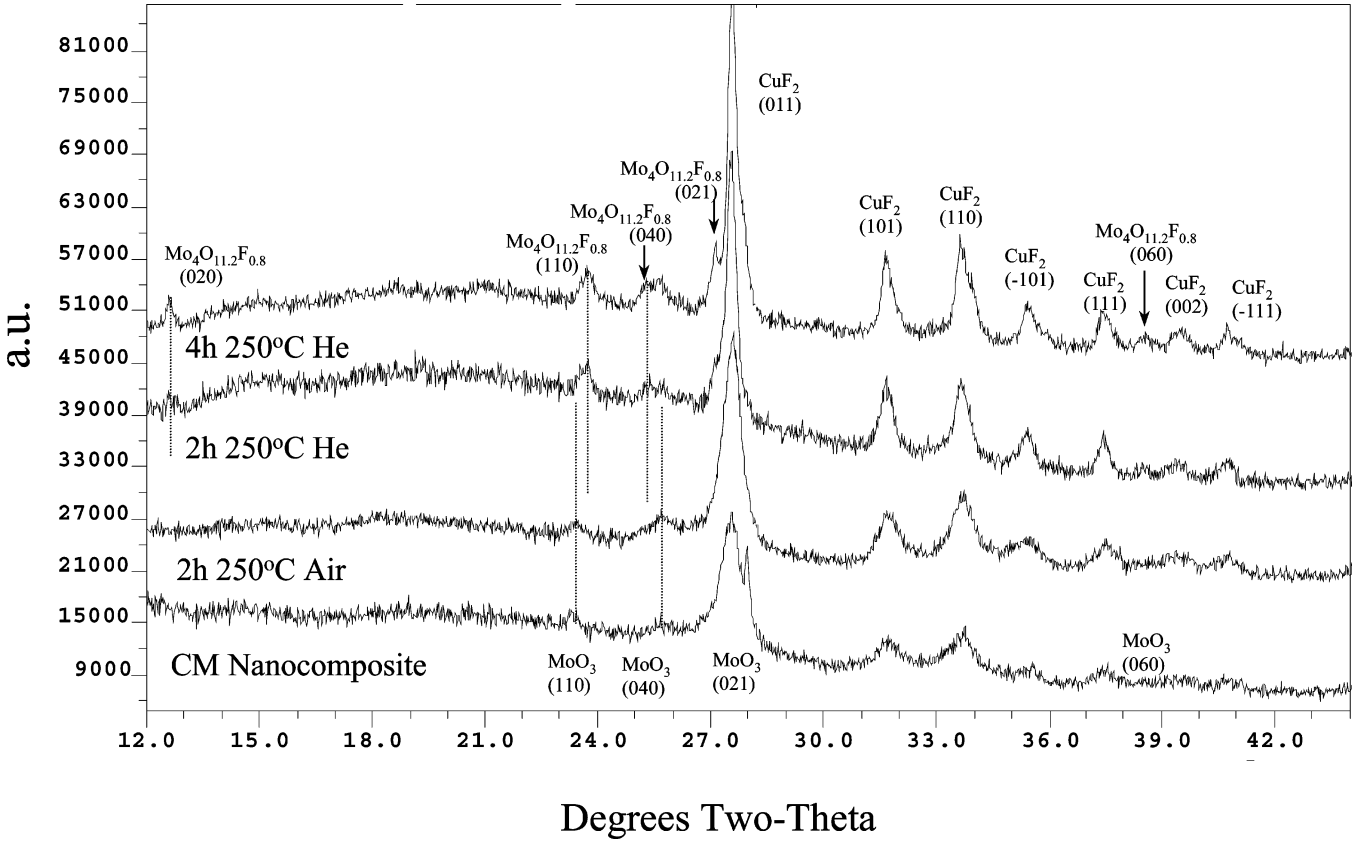

Figure 11. XRD patterns of CuF_2 MCM nanocomposites with various annealing treatments showing fluorination of the MoO_3 matrix.

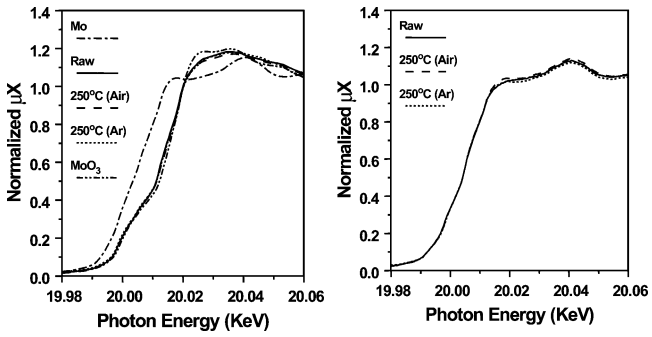

Figure 12. Mo K-edge XANES spectra of the CuF_2:15% MoO_3 nanocomposite in the as-prepared state (labeled raw), heated at 250 °C in air and argon (left panel), compared with XANES for Mo and MoO_3 and the reference Mo foil data used for calibrating the energy scale of the nanocomposite spectra (right panel).

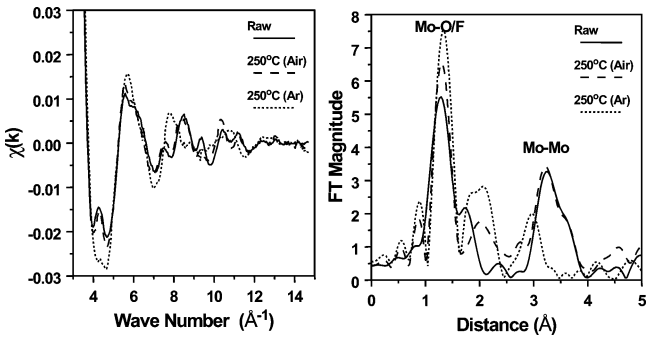

Figure 13. EXAFS spectra (left panel) and their corresponding phase-uncorrected Fourier transforms (right panel) for the CuF_2:15% MoO_3 nanocomposite in the as-prepared state (labeled raw), heated at 250 °C in air and argon showing significant structural modification after heating in Ar (FT range 3.5−14.3 $Å^{-1}$, k^3-weighted, and Hanning window of 1.0 $Å^{-1}$).

no structural change should be induced upon cation exchange, thereby effectively ruling out cation exchange as mechanism of structural modification. This leaves the distinct possibility that the change is induced by a partial anion exchange or extraction.

Anion exchange forming copper oxyfluorides without significant anion defect formation would raise the overall oxidation state of the Cu cation in contrast to the possible reduction experimentally observed by XANES. Anion exchange leading to the formation of $CuF_{2-2z}V_{(F)z}O_z$ with concomitant vacancy formation on the anion sublattice remains a distinct possibility but cannot be verified herein. Fluorine extraction through a reduction process would require the concomitant reduction of Cu^{2+} to Cu^{1+} to form $CuF_{2-\delta}$. Whereas X-ray photoelectron spectroscopy (XPS) gives no clear evidence of reduction, a possible oxidation state reduction is noted in the Cu K-edge XANES spectra (Figure 7), leading to an average oxidation state of approximately $Cu^{1.94+}$. One could argue that this is a result of surface defects present in large quantities in the interface regions of the 10 nm crystallites and not a bulk effect. However, the clear and consistent change in the longer range XRD data clearly supports a bulk effect. To gain more insight on this reaction, an analysis of the MoO_3 matrix was undertaken.

(d) Molybdate Matrix. Assuming an anion exchange or fluorine extraction via a solid-state redox process between the fluoride and oxide, we would expect to see a parallel fluorination of the molybdenum matrix and subsequent crystallographic and oxidation state changes. X-ray diffraction and absorption spectroscopy clearly reveal such distinct changes, especially upon annealing. High-energy processing in hardened steel containers bring the potential risk of Fe

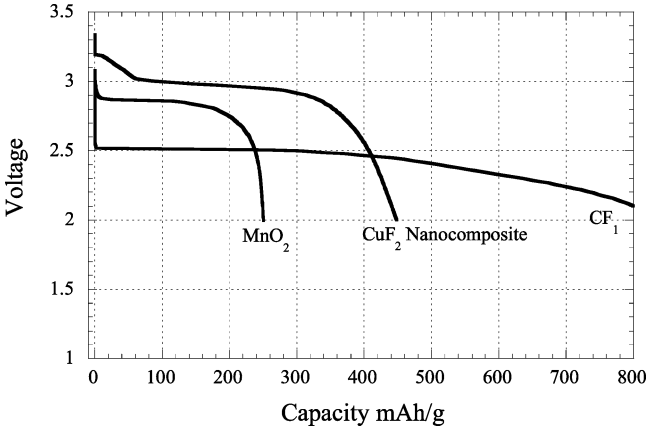

Figure 14. Specific capacity of CuF_2:MoO_3 nanocomposite vs that of MnO_2 and CF_1. Data were collected at 7.58 mA/g at 24 °C.

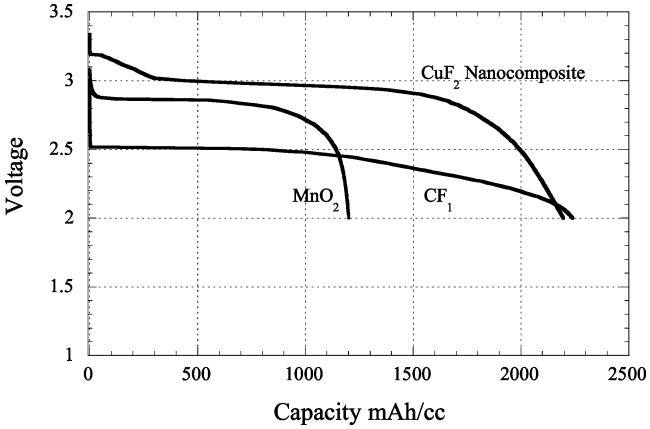

Figure 15. Voltage profiles comparing the relative performance of MnO_2, HT(CF_1), and CuF_2 positive electrodes. Tests were performed vs Li metal negative electrodes in 1 M $LiPF_6$ ethylene carbonate/dimethyl carbonate electrolyte at a rate of 7.58 mA/g at 24 °C. The calculated volumes are based on X-ray density (4.48 g/cm^3 MnO_2, 2.67 g/cm^3 CF_1, CuF_2 4.23 g/cm^3). All electrodes have discharged near theoretical capacities.

contamination (although very little was identified by X-ray fluorescence). To avoid any possible contribution of Fe, we fabricated the following samples, used for more detailed studies, in a high-energy planetary mill utilizing ZrO_2 HEM cells. It is interesting to note in Figure 10 that such materials are required to be annealed before full evolution of the electrochemical performance could be obtained. The highest specific capacities acquired for He annealed samples are equivalent to the theoretical capacity utilization of CuF_2 if the molybdenum-based matrix is considered to be inert. If indeed the matrix is electrochemically active and contributed to capacity (which is likely), the utilization of the CuF_2 is approximately 95%. The difference in annealing requirements for these nanocomposites, as discussed below, has its origins in the structural changes occurring because of the lower impact energy of the planetary high-energy milling technique.

Figure 11 shows the XRD pattern of the high-energy milled CuF_2 nanocomposite of 15% MoO_3 without postannealing. It shows very small Bragg reflections consistent with MoO_3 nanocrystallites; in addition, the color was very pale, indicating little reduction of the Mo^{6+} oxidation state. Upon annealing in air at 250 °C, the molybdate retains its Mo^{6+} character of MoO_3 (Figure 11), whereas upon annealing in He, the samples turn a darker color, and a clear transition of the Bragg peaks takes place, resulting in a phase consistent with $Mo_4O_{11.2}F_{0.8}$. This is readily apparent in the samples annealed for 2 and 4 h in He (Figure 11). The fluorination in the inert atmosphere resulting in the slight reduction of the Mo^{6+} oxidation state and improved conductivity is perfectly consistent with markedly improved performance observed in the inert vs air or nonannealed scenarios shown in Figure 10.

The Mo K-edge XANES data of the CuF_2:15% MoO_3 nanocomposite in the as-prepared state and after heating at 250 °C in air and argon are shown in Figure 12. The edge energies at half-height for the nanocomposite in the as prepared state, heated in air, and heated in argon are shifted by 7.7, 7.9, and 7.8 eV relative to Mo. The observed edge shift of the nanocomposite is intermediate to those observed for MoO_2 (6.3 eV) and MoO_3 (8.8 eV). Hence, the Mo oxidation state in the nanocomposite is between 4 and 6. On the basis of the edge shifts for MoO_2 and MoO_3, one could estimate that a unit change in formal valency should lead to an edge shift of 1.25 eV, approximately. On this basis, the average oxidation state of Mo in the nanocomposite is estimated to be 5.2. This is consistent with the formation of a molybdebum oxyfluoride, as described above. In this analysis, the effect of the electronegativity of O vs F, in the case of anion exchange, was neglected.

Comparisons of the EXAFS spectra and Fourier transforms of the nanocomposite in the as-prepared state and after heat treatment in air and argon are shown in Figure 13. The spectra display some changes in local coordination geometry occurred as a result of heat treatment, with the effect being most dramatic after heating in argon. An increase in the amplitude of the Mo−O contribution occurred after heating in air, with a further increase after heating in argon. The higher amplitude of the Mo−O interaction may be due to a higher degree of structural order as one would expect under annealing conditions. A second peak appears to emerge around 2 Å. The main Mo−Mo interaction appears to be slightly changed upon heating in air. The amplitude of this Mo−Mo interaction, however, is significantly reduced and shifted to a lower distance upon heating in argon. The progression of these structural changes is consistent with the evolution of the oxyfluoride upon annealing in Ar established by XRD.

The Mo K-edge XANES results are consistent with the slight reduction of the Mo^{6+} cation expected for the XRD identified $Mo_4O_{11.2}F_{0.8}$, which contains Mo with an average oxidation state of 5.8. Although XRD was consistent with $Mo^{5.8+}{}_4O_{11.2}F_{0.8}$, the molybdenum oxyfluorides can have a wide range of fluorination and therefore at this point it is next to impossible to ascertain the degree of extraction, as even with nanoprobe analysis we risk fluorine evolution from the samples. This is also complicated by the lack of sensitivity of XRD to completely amorphous phases and very fine nanocrystalline structures. Assuming an average Mo oxidation state of 5.2 determined by XANES, we would extend this solid solution and $CuF_{2-\delta}$ defect composition (assuming F abstraction) to

$$CuF_{1.94} + Mo_{0.12}O_{0.26}F_{0.10}$$

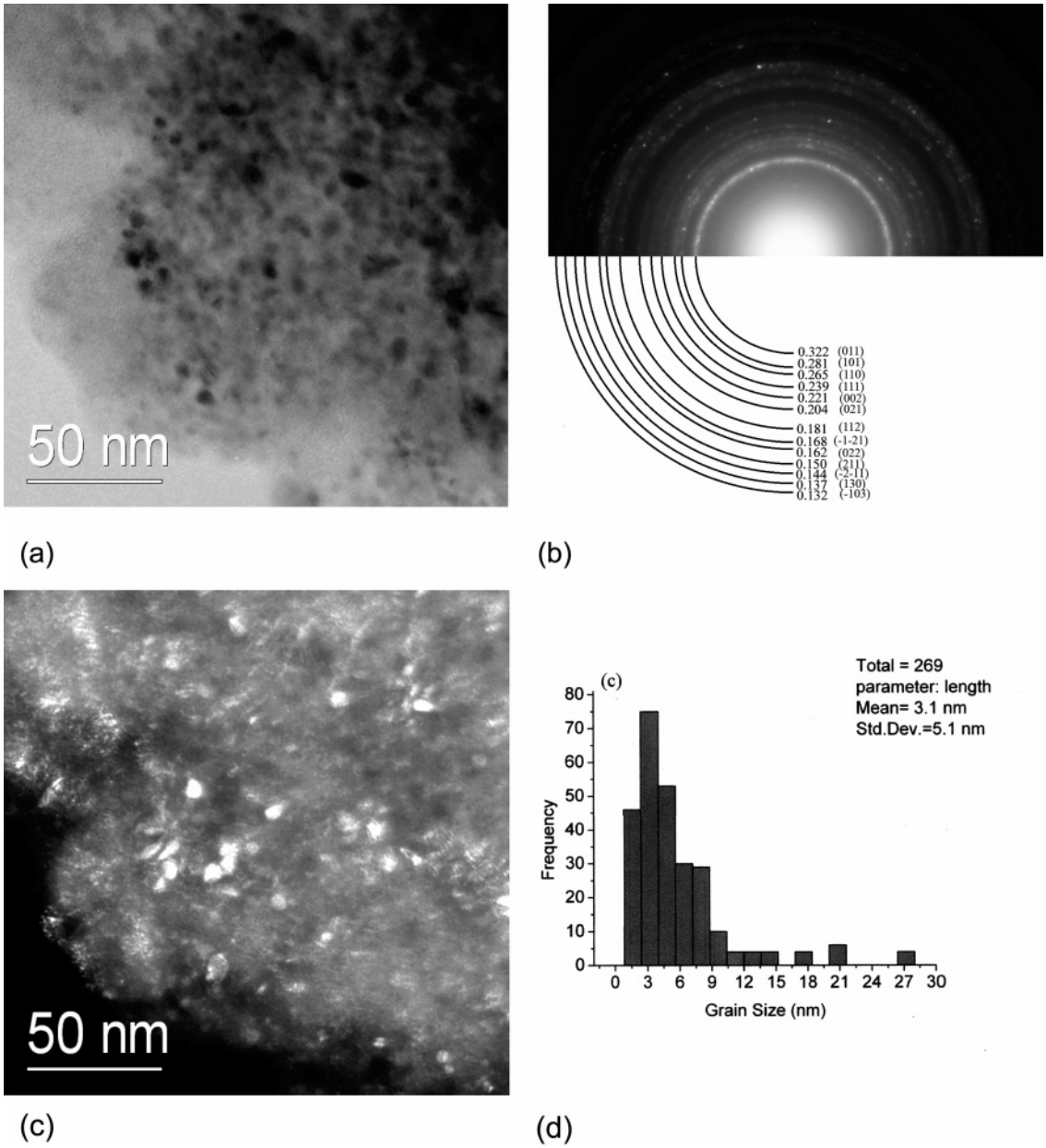

Figure 16. (a) Bright-field TEM image of CuF_2:7% MoO_3 nanocomposites showing a dense composite structure. The larger CuF_2 crystals are clearly visible. (b) Corresponding SAED pattern. The indices correspond to CuF_2 *P*21/*n*. (c) Tilted dark-field TEM image using an aperture centered on part of the most intense (011) reflection of CuF_2, where both CuF_2 and MoO_3 nanocrystals are clearly resolved. (d) The corresponding size distribution.

This accounting is based on the Cu K-edge and Mo K-edge XANES result of $Cu^{1.94+}$ and $Mo^{5.2+}$, respectively. Although a respectable match for the two calculated values, the actual F exchange amounts are slightly off in the molybdate ($F_{0.10}$ vs $F_{0.06}$). It is possible a very slight substitution of oxygen into the CuF_2 cocomittant with a nonstoichiometric vacancy formation may indeed occur to result in the nanocomposite

$$CuF_{1.9}O_{0.02} + Mo_{0.12}O_{0\cdot 26}F_{0.10}$$

(e) Electrochemical Performance. The practical advantages of the enabled CuF_2 nanocomposites are demonstrated in the comparison of the CuF_2:15% MoO_3 nanocomposite to the two predominant positive electrodes utilized in primary lithium batteries today, MnO_2 and CF_1. The former is utilized in relatively low-cost, high-rate lithium batteries, the latter for ultimate high specific energy batteries. Specific energy at discharge of 7.58 mA g^{-1} at 24 °C reveals a clear specific capacity advantage of CuF_2 MCM vs that of MnO_2 (Figure 14), and a definitive dominance of the CF_1 electrode vs the latter two (Figure 14). However, when taking into account volumetric energy density based on X-ray volume, CuF_2 MCM has a clear advantage over that of MnO_2 and CF_1 (Figure 15). Concerns regarding nanocomposite density are negated in mixed conducting matrix nanocomposites. Compressed pellet densities (utilizing 4% PVdF(HFP) binder and 5% carbon black pressed at 7000 psi to represent a realistically loaded electrode) of CuF_2 MCM (3.84 g/cm^3 for pellet composition) were identical (3.84 g/cm^3 for pellet composition) to that of compressed CuF_2 macro materials. The reason for this is that the MCM technology induces a dense composite (Figure 16) of low surface area (1 m^2/g) and does not have the intrinsic difficulties related to densification of

electrodes, processing, ambient and elevated temperature electrolyte reactivity, and possible health concerns that are associated with discrete nanomaterials. Quantitative distribution of the domains associated with the (011) reflection of the CuF_2 was utilized in the associated distribution figure, showing an average domain size of 3 nm with little population over 10 nm. This value is somewhat smaller than the 15−30 nm, as shown by XRD, possibly because of grain selection in the analysis. A surface grain was chosen for the clarity of image, grains closer to the surface are exposed to higher-impact energies during HEM. Finally, although very poor because of the oxidation of Cu into solution, some reversibility of this compound has been identified. Further details of the electrochemical performance and a more detailed nanocomposite distribution analysis will be addressed in a following paper.

4. Summary

Near theoretical capacity (450 mA h g^{-1} composite or 525 mA h g^{-1} pure) of CuF_2 has been enabled through the use of CuF_2 nanodomains within a small percentage of novel mixed conducting matrices. The best performance was identified for matrices consisting of MoO_3. Compared to pure CuF_2 or nanocomposites fabricated with carbon matrices, the oxide matrices induced a distinct crystallographic change to the CuF_2 monoclinic crystallites. This transformation manifested itself in the increase of the *b* and *c* lattice parameters, β angle and crystal volume as determined by XRD, a possible shrinking of the axial bonds of the CuF_6 octahedron as determined by EXAFS, and a slight reduction of oxidation state as indicated by XANES. In parallel, evidence for the formation of a molybdenum oxyfluoride was supported by XRD and XAS data, suggesting a solid-state redox reaction involving fluorine abstraction or exchange from CuF_2 to the oxide materials. The successful introduction of the mixed conducting matrices containing fast ion and electron transport enables the utilization of nanocomposites to increase the performance of charge-transport-challenged electrode materials. Such a technique that has previously shown success with negative electrode materials[32] can be applied to the enablement of a wide variety of metal fluorides or be extended to other less severely challenged positive electrode materials such as $LiMePO_4$. This is without the disadvantages of discrete electrode nanomaterials, which include poor volumetric efficiency, catalysis of parasitic electrolyte reactions at the surface, and possible safety concerns.

Acknowledgment. The authors thank the U.S. Government for the support of this research and J. Gural for technical assistance. A.N. Mansour also acknowledges financial support by the Carderock Division of the Naval Surface Warfare Center's In-house Laboratory Independent Research Program administrated under ONR's Program Element 0601152N. The National Synchrotron Light Source, Brookhaven National Laboratory, is supported by the U.S. Department of Energy, Office of Science, Office of Basic Energy Sciences, under Contract DE-AC02-98CH10886.

CM070421G

(32) Anani, A. A.; Crouch-Baker, S.; Huggins, R. A. *J. Electrochem. Soc.* **1988**, *135*, 2103.